

Studies of Perovskite Materials for High-Performance Storage Media, Piezoelectric, and Solar Energy Conversion Devices

Tingting Qi, Ilya Grinberg, Joseph W. Bennett,
Young-Han Shin, and Andrew M. Rappe
The Makineni Theoretical Laboratories, Department
of Chemistry, University of Pennsylvania,
Philadelphia, PA
{tqi, ilya2, bennett4, rappe}@sas.upenn.edu

Ka-Lo Yeh and Keith A. Nelson
Department of Chemistry, Massachusetts Institute
of Technology, Cambridge, MA
{kaloyeh, kanelson}@mit.edu

Abstract

Perovskite materials are crucial in a variety of important technological applications. Using quantum-mechanical simulations and accurate molecular dynamics models, we have computationally investigated ferroelectric materials for applications in computer memory, piezoelectrics and photovoltaics. By tuning the applied electric pulses' shaping and delay separation, we find the lower limit for tetragonal PbTiO_3 polarization switching time period is on the scale of 10 picoseconds. Structural and electronic properties of a semiconductor non-oxide perovskite BaZrS_3 are investigated in detail. We also microscopically model relaxor behavior demonstrated by the next generation piezoelectric devices, not only reproducing dielectric response but also revealing the significance of local crystal chemistry.

1. Introduction

There is a strong demand for perovskite oxides (formula ABO_3) with higher performance better functionality and performance for use in many different types of applications, such as sensing, data storage, and energy conversion. For example, perovskite solid solutions with high piezoelectric response are used in current and next-generation military SONAR devices. When deformed by the external underwater sound vibrations, a piezoelectric material generates an electric field. This is then interpreted to gain information about depth, distance, and the identity of the source of the sound.

The flexible structure of perovskites lends itself to a variety of applications, depending upon the choice of A- and B-site atoms. In particular, the relationship between the sizes of the A-O and the B-O₂ sub-lattices plays an important role in determining the properties of the

materials. This relationship is characterized by the tolerance factor (t) given by:

$$t = \frac{R_{\text{A-O}}}{R_{\text{B-O}}\sqrt{2}} \quad (1)$$

where $R_{\text{A-O}}$ is the sum of A and O ionic radii and $R_{\text{B-O}}$ is the sum of B and O ionic radii^[1]. Tolerance factor $t < 1$ usually leads to the rotation and expansion of the B-O₆ octahedra. Such octahedral rotations often generate a low temperature anti-ferroelectric phase (e.g., PbZrO_3). If $t > 1$, the B-O₆ octahedra are stretched from their preferred B-O bond lengths, promoting B-cation distortions by creating room for the B-cations to move off-center. Therefore, simple perovskites with $t > 1$ are usually ferroelectric.

For example, when Pb and Ti are paired as A and B respectively, these cations move in a concerted manner, so PbTiO_3 ($t=1.06$) is ferroelectric. Ferroelectric ABO_3 oxides are sensors in SONAR devices and are also useful for non-volatile random access memory (NVRAM) devices. When external underwater sound vibrations deform such a SONAR device material, it generates an electric field which can then be interpreted to gain information about depth and distance and the identity of the source of the sound. Ferroelectric random access memory (FeRAM) is one of a growing number of alternative non-volatile memories, as it offers lower power usage, faster write speed and a much greater maximum number of write-erase cycles.

If however, Ba and Zr are paired, the resulting perovskite oxide ($t=1$) is a dielectric with no polarization. Dielectric ABO_3 oxides are important to the wireless communication industry as components in electro-ceramic capacitors. Polarizable perovskites have also attracted attention as possible photovoltaic materials, as solid oxide solutions could efficiently separate photo-generating carriers via the bulk photovoltaic effect. The complexity of these multi-component systems is crucial for their high technological performance. It also creates

a large phase space in which compositional variations need to be further explored.

Highly-accurate modeling is necessary to understand the origin of the various properties exhibited by perovskites used in the current state-of-the-art technology, in order to speedup the design of new materials with enhanced performance for future devices. Over the last decade, first principles calculations have emerged as a vital tool for understanding complex solid state systems due to a combination of methodological improvements and faster computer speeds. In particular, density functional theory (DFT) is an extremely successful approach for the description of ground state properties of metals, semiconductors, and insulators^[2,3] due to a combination of accuracy and computational efficiency. Here, we report on our recent studies using both highly-accurate molecular dynamics models and DFT calculations. With PbTiO_3 as our prototype, we study the upper limit of the writing speed for FeRAM^[4]. Exploring new type of perovskites $\text{ABO}_{3-x}\text{S}_x$ paring O with S, we present the structural relaxation, vibrational analysis and dielectric response of BaZrS_3 ^[5]. Finally, we investigate the $\text{PbMg}_{1/3}\text{Nb}_{2/3}\text{O}_3$ - PbTiO_3 system, which forms the basis of the next-generation single crystal based SONAR devices^[6]. We study relaxor behavior which underlies the excellent piezoelectric properties of this material and show that local crystal chemistry, rather than long-range chemical inhomogeneity, is crucial.

2. Results and Discussion

2.1 Collective Coherent Control: Synchronization of Polarization in Ferroelectric PbTiO_3 by Shaped THz Fields

Coherent optical control over ultrafast molecular behavior, including chemical reactions, has been explored in recent years^[7]. This has been spurred by the application of optimal control theory and related methods^[8,9] and by the development of femtosecond pulse shaping techniques^[10-12] through which complex optical waveforms have been crafted and optimized to induce specified molecular responses. Here, we model theoretically the extension of coherent control to collective structural change.

Perovskite ferroelectric crystals have simple collective lattice vibrational modes that describe the microscopic pathways along which structural change occurs (see Figure 1a). For this reason, these crystals are prototypes for the study of collective structural rearrangements, with many modeling studies investigating both static and dynamic aspects of their phase transitions^[13,14]. A particularly important aspect is domain switching, the process of reorienting a part or all

of a domain so that its macroscopic polarization points in a different direction. We and others^[15,16] have sought to illuminate how microscopic inter-atomic interactions affect the rate and the mechanism of ferroelectric domain switching.

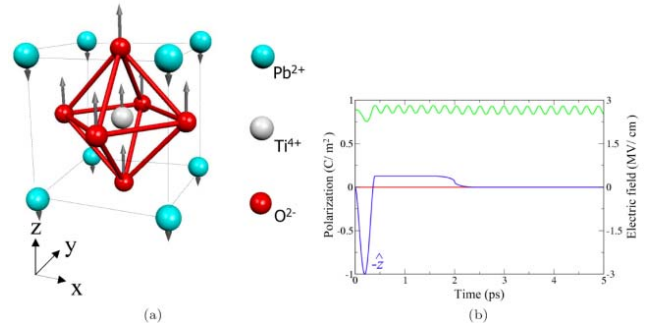


Figure 1. (a) PbTiO_3 unit cell in the tetragonal ferroelectric phase, with a +z domain orientation. The soft vibrational mode is indicated by the arrows on the ions. (b) Time-dependent lattice response to a single asymmetric THz pulse (electric field shown in blue) with its large lobe polarized along the -z direction, i.e., “anti-parallel” to the static ferroelectric polarization. The z-component P_z (shown in green) oscillates about its static nonzero value as the Ti and other ions oscillate about their lattice positions in the +z domain. No significant responses of the other components P_x and P_y (shown in black and red respectively) about their static values of zero are induced.

In the tetragonal phase of lead titanate (PbTiO_3 , PTO), the crystal has two domain orientations characterized by opposite polarization directions along the tetragonal axis with symmetrically equivalent ground states separated by an energy barrier. The polarization direction can be reversed under an electric field. This is exploited extensively in ferroelectric memory devices, so the dynamics of domain switching have been of technological as well as fundamental interest. There is great experimental interest in rapid ferroelectric polarization switching under strong electric fields, with most experimental approaches limited to the thin film regime^[17-21]. Most studies of polarization reversal focus on domain wall properties and dynamics under the influence of an electric field that is applied through electrodes at the sample surfaces^[15,22,23]. Earlier attempts to control crystalline soft modes and phase transitions through impulsive stimulated Raman scattering used non-resonant optical pulses without tailored pulse profiles^[24-26] and were based on simple models for the impulsively driven lattice vibrations and the crystalline responses to them. So far such attempts have failed to find experimental validation because the high light intensities needed to reach sufficient vibrational amplitudes far exceed typical material damage thresholds.

In contrast, here we explore the fundamental limit of the polarization switching time of ferroelectric PTO under the coherent control of a terahertz-frequency

electromagnetic driving field that permeates the sample and is resonant with its soft mode frequency. Using a well validated atomic potential model of PTO^[15,27], we consider the coherent reorientation of a large region, without domain wall formation or movement. We study a terahertz-frequency driving field with tailored amplitude, phase, and polarization profiles, motivated by recent progress in the generation of large amplitude shaped terahertz fields and in the observation of anharmonic responses of ferroelectric soft modes to such fields^[28]. We examine the possibility of coherent control over domain reversal to “read” or “write” bulk ferroelectric data storage media on picosecond time scales.

We carried out molecular dynamics (MD) simulations with $6 \times 6 \times 6$ supercell using the bond-valence (BV) model, which reproduces the ferroelectric behavior accurately with a simple interatomic potential parameterized to DFT calculations^[27]. BV simulations show a ferroelectric transition at 575K with a mixed order-disorder and displacive phase transition character^[14]. Important results have been achieved with this model, including identification of the nucleation and growth mechanism of the 180° domain wall of PTO under an external electric field^[15] and correlations between the structure and the dielectric properties of Pb-based relaxor ferroelectrics^[29].

To simulate THz experiments, one or more electric field pulses were applied to the system. All pulses had an asymmetric electric field profile with a large amplitude lobe of short duration (a full width at half maximum of ≈ 150 fs, to include frequency components up to about 6.6 THz) and a lower amplitude lobe of longer duration in the opposite polarity. The electric field integrates to zero as required for optical pulses (Figure 1b). The asymmetric field profile is well suited for driving nonlinear responses in the direction of the large amplitude lobe.

To switch the polarization from $+\hat{z}$ to $-\hat{z}$, the most direct way is to apply electric field pulses along $-\hat{z}$. Figure 1b shows that applying a $-\hat{z}$ -oriented electric field pulse causes the z component of the polarization (P_z) to oscillate in time about its nonzero static value. The other polarization components (P_x and P_y) remain essentially zero. The oscillation period of about 240 fs, which corresponds to 4.2 THz, is independent of pulse magnitude, indicating an essentially harmonic mode (the Pb-O or so-called Last mode) at these amplitudes. The phonon frequency is in good agreement with DFT calculations and the experimental value^[30] of 4.5 THz.

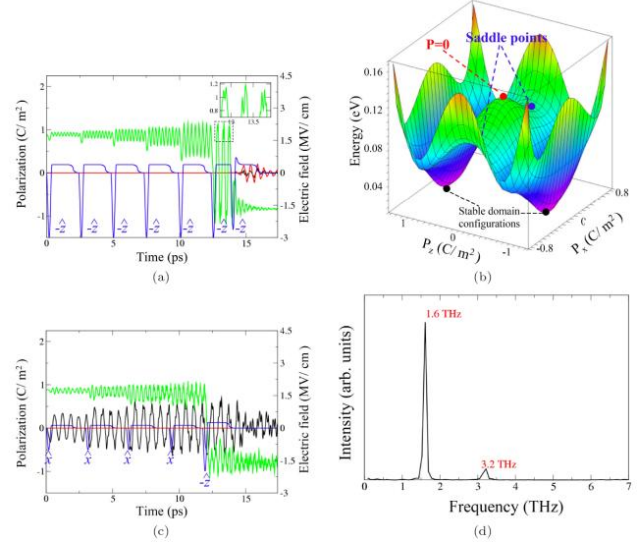


Figure 2. Collective coherent control over ferroelectric polarization with shaped terahertz waveforms. (a) Sequence of seven asymmetric THz pulses (electric field in blue), all z -polarized with large lobes (3 MV/cm) along the $-\hat{z}$ -direction. Induced response of polarization z -component P_z (in green) shows oscillations at the soft mode frequency. (b) Lattice potential energy surface (PES) with respect to P_x and P_z , calculated using the BV model. A PES local maximum appears at the high-symmetry cubic structure with $P_x=P_z=0$. The z -polarized THz field in (a) drives the system over this potential energy barrier. Domain switching can occur with lower energies along trajectories that pass through or near the saddle points in the PES. (c) Sequence of four THz pulses with \hat{x} -oriented fields followed by a final THz pulse with $-\hat{z}$ -oriented field. (d) Power spectrum from Fourier transformation of P_x and P_z in (c). A strong peak stems from P_x oscillations at the 1.6 THz phonon frequency. The smaller peak shows the second harmonic frequency of oscillations in P_z .

In order to reorient the lattice polarization, the coherent vibrational amplitude must be large enough to overcome the potential energy barrier between the two stable polarization states. Depending on the timing, the P_z vibrational coherence could be reduced or enhanced by successive pulses. As shown in Figure 2a, polarization reversal can be achieved within 15 ps with six appropriately timed pulses of amplitude 3 MV/cm. In order to suppress coherent return of the polarization to its original direction and multiple successive domain flipping events, we applied one additional $-\hat{z}$ -oriented pulse out of phase with the P_z oscillations. This guaranteed that after the system crossed the barrier, it remained trapped in the desired polarization state. At 0K, one out-of-phase pulse reliably leaves the domain completely flipped. It is also important to note that the out-of-phase pulse cools down the system substantially (≈ 95 K), since much of the energy is in the coherent mode after the first six pulses. In order to avoid excessive heating of the system, such an out-of-phase pulse could be useful not only at 0K but also at finite temperature.

It is well known that polarization rotation offers lower energy pathways to polarization flipping than directly surmounting the local potential energy maximum at the high-symmetry cubic lattice configuration. Atomistically, polarization rotation corresponds to a trajectory for Ti that goes around, rather than through, the unit cell center^[31]. We therefore investigated prospects for maintaining soft mode vibrational coherence while undergoing trajectories of this sort. This alternative scheme involves significant ionic motions and lattice polarization components along the \hat{x} and/or \hat{y} directions as well as \hat{z} , with the system exploring much more of the three-dimensional lattice potential energy surface (PES). Figure 2b shows the lattice potential energy obtained from the BV model as a function of P_z and P_x . The energies required to reach the high-symmetry PES local maximum and a saddle point (ΔE_z and ΔE_x , respectively) are compared in Table 1. The saddle point energy is about 20% lower, offering lower energy switching trajectories than those that pass through the PES maximum.

Table 1. Comparison of potential energy local maximum ΔE_z vs. saddle point ΔE_x for polarization switching in PTO

| | DFT | BV model |
|-----------------------------|-------|----------|
| ΔE_z (eV/unit cell) | 0.168 | 0.143 |
| ΔE_x (eV/unit cell) | 0.136 | 0.110 |
| $\Delta E_x/\Delta E_z$ | 0.81 | 0.77 |

In order to explore coherent control of domain switching with trajectories that go around rather than through the PES maximum, we conducted MD simulations with sequences of \hat{x} - and \hat{z} -polarized asymmetric terahertz pulses rather than all \hat{z} -polarized pulses as described earlier. Figure 2c shows an example with four \hat{x} -polarized pulses (with large lobes of amplitude 1 MV/cm along $+\hat{x}$) followed by one \hat{z} -polarized pulse (with a large lobe of amplitude 2 MV/cm along $-\hat{z}$). After a single \hat{x} -oriented pulse, the simulation shows that both P_x and P_z oscillations were excited, corresponding to polarization rotation in the $\hat{z}\hat{x}$ plane. The power spectrum in Figure 2d shows that the frequency for P_z oscillation was twice that of P_x (1.6 THz), which is a consequence of the lattice symmetry about the $x=0$ plane. The curvature of the PES draws the z -component of the polarization toward smaller values when the x -component undergoes an excursion toward positive or (symmetry-equivalent) negative values. For example, the Ti ion moves toward the $z=0$ plane when it is displaced in either direction from the $x=0$ plane. Thus each half-cycle of P_x corresponds to a full cycle of P_z . The oscillation amplitude of P_z depends quadratically on that of P_x until highly anharmonic regimes are reached,

and the P_z response would give rise to z -polarized frequency-doubling of x -polarized incident THz radiation.

The simulation results in Figure 2c show that each successive x -polarized pulse increases the lattice polarization rotation amplitude, as each time P_x reaches a maximum excursion away from zero, P_z reaches a maximum excursion away from its initial nonzero value toward a smaller value. After the fourth \hat{x} -oriented pulse, P_x exceeds P_z at the extrema of oscillation, which means that the polarization is rotating more than 45° and approaching the saddle point of the PES. Finally, a $-\hat{z}$ -oriented pulse is applied to push the system over the saddle point. This approach (Figure 2c) switches the ferroelectric domain more efficiently than the former method (Figure 2a), in terms of the number of pulses, their peak magnitudes, and their integrated energy. The result illustrates the value of shaping the polarization as well as the amplitude and phase profile of the terahertz control field. Polarization shaping has proved valuable in some examples of molecular coherent control with visible light fields as well^[28].

Maintaining coherence at finite temperature is more challenging than at 0K, because the increase in random fluctuations makes the final state more difficult to predict. The increased temperature changes several key factors that affect the switching process. First, coherence is lost more rapidly due to faster energy dissipation and pure dephasing. Second, the ferroelectric well depth decreases with temperature, as the higher entropy of the paraelectric state makes its free energy more competitive with that of the ferroelectric state. These two effects compete, with the first inhibiting coherence and the second facilitating domain flipping.

To guide our understanding of finite temperature domain switching, we concentrate on the response of the domain to a single $-\hat{z}$ -oriented pulse. For a single pulse to reorient the polarization, the pulse strength should be sufficient for the system to visit the energy minimum of the opposite polarization, yet not strong enough for the polarization to flip back. Shorter dissipation times can help to remove the excess energy from the soft mode by coupling the polarization with other modes. Our findings are summarized in Figure 3. Due to thermal fluctuations, the same initial conditions can yield different results, with flipping success being a probabilistic event. We chose four different initial sample temperatures (50, 100, 200, and 300K) to analyze statistically. For each temperature, we traced 250 trajectories starting from different equilibrated states irradiated by a single $-\hat{z}$ -oriented pulse. To avoid excessive heating of the material, we limited the amplitude of the short duration electric field lobe. In Figure 3, the circles indicate the probability that the system climbs over the PES barrier before damping reduces the energy in the coherent mode to below the barrier height (flip), and diamonds indicate the probability

that it crosses back to the original domain orientation (flipback). Hence, the difference between these two datasets is the probability of exactly one flip reversing a domain. Equation 1 fits the simulation results well (the fitting parameters are presented in Table 2):

$$\mathcal{P}(E, T, n) = \frac{1}{2} + \frac{1}{2} \tanh\left(\alpha\left[\frac{E}{E_0} - 1\right]\right) \quad (2)$$

where α and E_0 depend on temperature (T) and n . The E_0 values for both “flip” ($n=1$) and “flipback” ($n=2$) decrease monotonically with T . $E_0(T, 1)$ closely tracks the T -dependent free energy barrier, while the $E_0(T, 2)$ is higher than $E_0(T, 1)$ because of damping within one-half period. This effect nearly doubles the range of field amplitudes over which single flipping is achieved as T is raised from 50K to 300K. The trends from MD simulations illustrate well the competing effects introduced by temperature. We find the required minimum magnitude of the pulse decreases as the temperature increases because of the decreasing ferroelectric double well depth. Meanwhile, the range of pulse magnitudes that achieve “flip” without “flipback” is larger at higher temperatures because of increased dissipation.

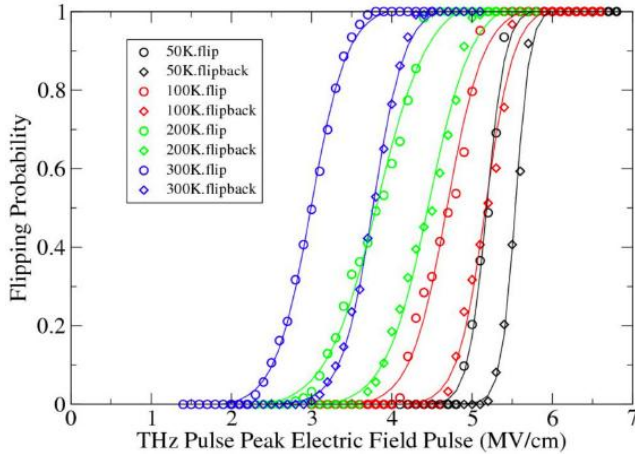


Figure 3. The probability of at least a single “flip” or at least two flips (denoted “flipback”) of polarization in response to a single $-\hat{z}$ -oriented pulse with varied peak field amplitudes at different temperatures. At higher temperatures, lower field amplitudes are sufficient to flip the domain, while stronger dissipation in the new domain suppresses flipback for a wider range of field amplitudes.

Table 2. Fitting parameters of flipping probabilities at different finite temperatures according to Equation 1. Temperature is in Kelvin and parameter α is unitless and field E_0 is in MV/cm.

| Temp | $\alpha(T, 1)$ | $\alpha(T, 2)$ | $E_0(T, 1)$ | $E_0(T, 2)$ | $E_0(T, 2) - E_0(T, 1)$ |
|------|----------------|----------------|-------------|-------------|-------------------------|
| 50 | 22.43 | 30.75 | 5.18 | 5.54 | 0.36 |
| 100 | 11.25 | 16.03 | 4.68 | 5.16 | 0.48 |
| 200 | 8.32 | 11.39 | 3.78 | 4.43 | 0.65 |
| 300 | 6.64 | 9.51 | 2.99 | 3.76 | 0.77 |

Through accurate MD simulations, we have demonstrated that collective coherent control over ferroelectric domain orientation should be possible through the use of shaped THz pulse sequences. Our results show that shaping of all aspects of the THz fields—the amplitude, phase, and polarization profiles—can contribute substantially to coherent control over collective material dynamics and structure.

2.2 The Effect of Substituting of S for O: The Sulfide Perovskite BaZrS₃

The impact of the chemical changes on the anion site in perovskites (e.g., substitution of S for O) has been largely unexplored. While sulfur analogs of some perovskite oxides have been synthesized^[32–34], these often contain impurity phases that prevent the elucidation of the electronic structure and the dielectric properties of the majority perovskite sulfide phase^[35,36]. To our knowledge, density functional theory calculations have not been used to model these materials. We use first-principles DFT calculations to study the atomic structure, the electronic structure and dielectric properties of BaZrS₃ and compare these to the properties of the oxide analog BaZrO₃.

We use an in-house solid state DFT code, BH (used in previously published studies^[37,38]) to relax ionic positions. We optimize super-cell lattice constants using the ABINIT software package^[39]. All relaxations are performed with a plane-wave cutoff of 50 Ry, using the local density approximation (LDA) of the exchange correlation functional and a $4 \times 4 \times 4$ Monkhorst-Pack sampling of the Brillouin zone^[40]. The response function and Berry phase polarization calculations are performed with a $6 \times 6 \times 6$ grid was used^[41]. We represent all atoms by norm-conserving optimized^[42] designed nonlocal^[43] pseudo-potentials, generated with the OPIUM code^[44].

We use a $2 \times 2 \times 2$ super-cell to model any possible three-dimensional (3D) perovskite tilt system^[45–47] for both BaZrS₃ and BaZrO₃. Our previous DFT calculations have found that the ground state of BaZrO₃ is a $2 \times 2 \times 2$ supercell with a Glazer tilt system $a^-b^-c^-$ and $P\bar{1}$ symmetry^[38]. For BaZrS₃, the ground state structure exhibits the $\bar{a}^-a^+a^-$ tilt system and $Pnma$ symmetry, which agrees with experiment^[33]. The lowest energy lattice constants and atomic positions show good agreement with published experimental data, as shown in Table 3.

Table 3. Comparison of experimental^[33] and theoretical structural parameters for BaZrS₃. Shown first are the lattice constants along *a*, *b*, and *c* in Å, followed by the reduced coordinates of the atoms not located at high symmetry *Pnma* positions.

| | Experiment | Theory |
|----------------|------------|---------|
| <i>a</i> | 7.06 | 7.09 |
| <i>b</i> | 9.98 | 9.99 |
| <i>c</i> | 7.03 | 7.08 |
| Ba(<i>x</i>) | 0.0376 | 0.0517 |
| Ba(<i>z</i>) | 0.0069 | 0.0146 |
| S1(<i>x</i>) | -0.0045 | -0.0034 |
| S1(<i>z</i>) | 0.5614 | 0.5656 |
| S2(<i>x</i>) | 0.2155 | 0.2066 |
| S2(<i>y</i>) | -0.0293 | -0.0338 |
| S2(<i>z</i>) | 0.7869 | 0.7952 |

The ground state structure of BaZrS₃ is anti-ferroelectric with significant Ba displacements. This is consistent with the tolerance factor $t=0.95$ obtained from the Ba⁺², Zr⁺⁴, and S⁻² ionic radii. This is in contrast to BaZrO₃ ($t=1$) which exhibits paraelectric behavior for all temperatures. The antiferroelectric pattern of cation displacements in BaZrS₃ is different from that found in the classic anti-ferroelectric PbZrO₃ (PZO). In PZO, octahedral rotations in the $\bar{a}^- \bar{a}^- c^0$ tilt system (*Pbam* symmetry) permit concerted cation displacements along (111) direction^[48]. In BaZrS₃, the displacements allowed by the tilt system are along (101) direction, instead of (111), as the in-phase tilts along *b* prevent A-cations from moving along *b* (Figure 4b), while allowing motion along *a* and *c*. The average displacements are much larger for Ba ions (0.35 Å (0.07 Å)). The strong Ba displacements are due to the large volume of S₁₂ cages compared to the O₁₂ cage in BaZrO₃. The ionic radius of S⁻² is 1.3 times larger than that of O⁻². Even for simple metal cations with no stereochemically-active lone pairs, a large increase in the A-site volume relative to the size of the A-cation has been shown to give rise to large off-center distortions.

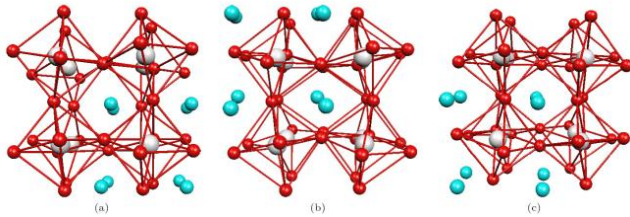


Figure 4. Shown here is the relaxed 2×2×2 BaZrS₃ supercell. Ba is blue, Zr is gray and S is red. The tilt angle of S₆ cages, 12.2°, is out of phase along *a* (a) and *c* (c), and in phase along *b* (b). This indicates *Pnma* symmetry, which agrees with experiment.

The Born effective charges of Ba and Zr ions are affected by the large displacements and volume in BaZrS₃. The isotropic ground state structure of BaZrO₃ means that the diagonal elements of the effective charge

tensor are all the same for all of the atoms of a given species (Table 4). However, in BaZrS₃ the AFE cation displacements break symmetry and cause the effective charge for motion in the \hat{x} and \hat{z} directions to be different than the effective charge for \hat{y} , the direction of the smallest displacement.

Table 4. Average diagonal values of the transverse and longitudinal effective charge tensors for each element. The longitudinal components of effective charge are the transverse components divided by ϵ_{∞} , and show that BaZrS₃ has a more covalent character than BaZrO₃. Shown first are values of BaZrO₃, then for BaZrS₃, which had a greater range of values for the diagonal elements.

| species | $Z_{xx}^{*(T)}$ | $Z_{yy}^{*(T)}$ | $Z_{zz}^{*(T)}$ | $Z_{xx}^{*(L)}$ | $Z_{yy}^{*(L)}$ | $Z_{zz}^{*(L)}$ |
|---------|-----------------|-----------------|-----------------|-----------------|-----------------|-----------------|
| Ba | 2.66 | 2.66 | 2.66 | 0.54 | 0.54 | 0.54 |
| Zr | 6.08 | 6.07 | 6.10 | 1.24 | 1.24 | 1.24 |
| O1 | -2.09 | -2.09 | -4.57 | -0.43 | -0.43 | -0.93 |
| O2 | -2.10 | -4.54 | -2.10 | -0.43 | -0.93 | -0.43 |
| O3 | -4.55 | -2.10 | -2.09 | -0.93 | -0.43 | -0.43 |
| Ba | 2.81 | 2.92 | 2.81 | 0.29 | 0.30 | 0.29 |
| Zr | 7.22 | 7.56 | 7.20 | 0.75 | 0.79 | 0.75 |
| S1 | -2.44 | -2.07 | -5.38 | -0.25 | -0.22 | -0.56 |
| S2 | -2.20 | -6.33 | -2.19 | -0.23 | -0.66 | -0.23 |
| S3 | -5.39 | -2.07 | -2.44 | -0.56 | -0.22 | -0.25 |

While the $Z^{*(T)}$ values of Ba are similar for BaZrO₃ and BaZrS₃, the values for Zr are increased by the substitution of S for O. The lower electro-negativity of S anions makes the Zr-S bonds more covalent than the Zr-O bonds, increasing the magnitudes of the Born effective charge of Zr and S.

Our dielectric response calculations (ϵ) find that the ionic part ϵ_{μ} of the BaZrS₃ dielectric constant ($\epsilon_{\mu}=36$) is 20% smaller than that for BaZrO₃ ($\epsilon_{\mu}=45$). While the Born effective charges are larger in BaZrS₃ than in BaZrO₃, the volume is larger and the mode displacements are smaller, due to antiferroelectric displacements of the Ba cations. This makes the effective charges of the vibrational modes lower leading to a decreased dielectric constant.

Unlike the ionic part, the high frequency component of the dielectric response is stronger for BaZrS₃ ($\epsilon_{\infty}=9.6$) than for BaZrO₃ ($\epsilon_{\infty}=4.9$). The greater covalency of Ba-S and Zr-S bonds gives rise to greater response by the electrons to the applied electric field. The total dielectric constant is a sum of the ionic and the high-frequency components and is slightly smaller for BaZrS₃ ($\epsilon_{\text{tot}}=46$) than for BaZrO₃ ($\epsilon_{\text{tot}}=50$).

We investigate the electronic structure of BaZrS₃ using orbital-resolved projected density of states (PDOS) analysis (Figure 5b) and compare it with PDOS of BaZrO₃ (Figure 5a).

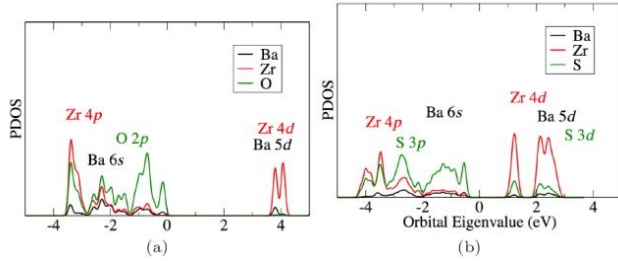


Figure 5. Projected density of states (PDOS) analysis shows that the electronic structure of BaZrO₃ (a) differs greatly from BaZrS₃ (b). Contributions from Ba are labeled in black, Zr in red and O in green.

The peaks in BaZrS₃ are more diffuse, indicating more covalent bonding with greater mixing between the cation and anion states. For both materials the valence band consists of mainly anion *p* states.

The conduction bands of the two materials show some differences. In BaZrS₃ the conduction band includes states with some S 3*d* character, indicative of the covalent nature of the Zr-S bonds in BaZrS₃. The mixing between the S 3*d* and *p* states lowers the energy of the valence band. Such mixing of *d*-states does not occur in BaZrO₃, as O does not contain *d*-orbitals close enough in energy to mix. The conduction band is therefore located at lower energy in BaZrS₃ than in BaZrO₃, lowering the DFT band gap from 3.9 eV (BaZrO₃) to 1.7 eV (BaZrS₃).

The substitution of S for O creates a band gap that is closer to the energy range of the visible light spectrum, providing a scheme in which ABX₃ materials could potentially be used for photovoltaic conversion devices. We have performed the first DFT study of BaZrS₃, investigating structural, dielectric and electronic properties, and find that in contrast to the para-electric oxide analog BaZrO₃, the ground state structure of BaZrS₃ is anti-ferroelectric, with larger Ba displacements. The dielectric constant of BaZrS₃ is similar to that of BaZrO₃. Electronic structure of BaZrS₃ shows significant mixing between the low-lying S 3*d* and cation *d* states, leading to a lower conduction band energy and a low 1.7 eV band gap. Our findings suggest that sulfide ferroelectrics can be a promising direction for the exploration of new semiconductor ferroelectrics with tailorable properties.

2.3 A Molecular Dynamics Study of Dielectric Response in a Relaxor Ferroelectric

Perovskite relaxor ferroelectrics play an important role in technological applications and are of fundamental scientific interest due to their fascinating physical and

dielectric properties. The hallmark of relaxor behavior is the appearance of dielectric response dispersion and the deviation of the temperature dependence of the inverse dielectric constant ($1/\epsilon$) from the Curie-Weiss law (Figure 6a)^[49] below the so-called Burns temperature T_b . Phenomenological modeling of the frequency dependence of the dielectric constant ϵ shows a broad range of relaxation times and a divergence of the longest relaxation times close to T_c ^[50,51]. The dynamics of the relaxor phase in these materials are poorly understood at an atomistic level.

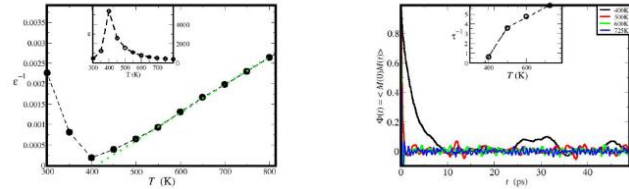


Figure 6. (a) Inverse static dielectric constant versus temperature obtained from 0.75PMN-0.25PT MD simulations (black). Linear extrapolation of high temperature data (dotted) allows us to estimate the T_c , which is larger than the $T_{c,max}$. Dielectric constant dependence on temperature is shown in the inset. (b) Time autocorrelation function $\Phi(t)$ for temperatures below and above the Burns transition. Extrapolation of the short time decay constant τ is shown in the inset.

To study relaxor behavior, we choose the technologically important PMN-PT relaxor at $x=0.25$. To simplify the analysis of the results, we study a full “random site”^[52] B-cation ordering. In this case, the *B'* is populated by Nb only, while the *B''* sites is populated randomly by an equal proportion of Mg and Ti, with the *B'* and *B''* arranged in a rocksalt order. We perform molecular dynamics simulations on a 6×6×6 super-cell using a first-principles derived atomistic bond-valence model. The simulations are run for 1–2 ns, and the local and total polarization of the super-cell evaluated at each time-step, allowing us to extract the dielectric response at the GHz.

Static bulk response: Analysis of the polarization fluctuation data obtained by the simulation shows that that our system exhibits all of the features of the experimentally observed PMN-0.25PT dielectric response. For example, the static dielectric constant displays a deviation from the Curie-Weiss ϵ temperature dependence at the Burns temperature T_b of 500K and peaks at $T_{c,max}$ of 400K (Figure 6a). A fit to the high-temperature inverse dielectric constant data results in a Curie constant $C=1.5 \times 10^5$ K and a T_c of 415K (obtained by extrapolation to $1/\epsilon=0$). Comparison with the experimental values ($T_{c,max}=400$ K, $T_c=440$ K, $T_b=520$ K,

$C=1.3 \times 10^5$) for PMN-0.20 PT composition shows that our results are in good agreement with experiment.

Frequency-dependent imaginary bulk response: We now examine the frequency dependence of the dielectric response, in particular the dielectric loss (Figure 7a). This is evaluated using the Laplace-Fourier transform of the polarization time autocorrelation function $\Phi(t)$. Comparison with the experimental dielectric spectroscopy results of Bovtun et al.^[51] shows good agreement between the experiment and our simulations for several features of the dielectric response. For $T > T_b$, both simulation and experiment find only one dielectric loss mode at 1–2 THz (soft mode), which decreases in frequency until T_b . For $T < T_b$, this mode's frequency slowly increases as temperature is lowered. The contribution of this mode to the overall dielectric loss is always between 100 and 200, small compared to the total dielectric constant of 6,000.

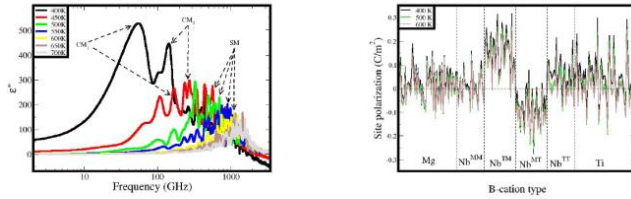


Figure 7. (a) Dielectric loss versus frequency for series of temperatures. Below the Burns temperature, two new loss peaks rapidly move into the GHz region as the temperature is lowered. (b) Average polarization for the B-cation sites. Sites 1–54 are Mg, sites 55–82 are Nb^{MM} , sites 83–109 are Nb^{TM} , sites 110–136 are Nb^{MT} , sites 137–162 are Nb^{TT} , and sites 163–216 are Ti. Average polarizations change slightly with lower temperature.

At $T < T_b$, the dominant contribution to the dielectric constant is due to two new modes which appear at T_b (called central modes in Reference 13). These appear at significantly lower frequencies compared to the soft mode and then are red-shifted as temperature is decreased. The shifts of the central modes to lower frequencies lead to the experimentally observed trend of the dielectric loss peak shifting rapidly to lower frequencies with lower temperature. The fact that simulations of a small super-cell can reproduce the experimentally observed relaxor dielectric response shows that local Å-scale phenomena are the origin of relaxor behavior.

Time-dependent individual atom response: We now examine the role of the individual B-cation pairs. Here, we focus on the identity of the nearest B-cation neighbors, which is the simplest possible variation in the B-cation local environment. Because of the random-site ordering, there are only six possible combinations of the two B-cation neighbors along a given Cartesian axis, All Mg and Ti atoms have two Nb neighbors. The Nb atoms are divided into four groups: those with two Mg neighbors (Nb^{MM}), those with two Ti neighbors (Nb^{TT}), those with Ti on the left and Mg on the right (Nb^{TM}), and those with Mg on the left and Ti on the right (Nb^{MT}). In our case, the

super-cell contains 54 Mg sites, 25 Nb^{MM} sites, 29 Nb^{TM} sites, 29 Nb^{MT} sites, 25 Nb^{TT} sites, and 54 Ti sites.

We examine the time autocorrelation functions for the individual site dipole moments ($\Phi(t)_i$), focusing on the $\Phi(t)_i$ initial decay lifetimes (τ_i). A large value of τ_i indicates slower relaxation dynamics and a stronger memory and is generally correlated with high amplitude and long period of $\Phi(t)_i$ oscillations at large t .

Analysis of τ_i data shows that relaxor behavior is nucleated at the Nb^{TT} sites. In the paraelectric phase at 725K, all sites exhibit fast relaxation ($\tau_i \approx 0.2$ ps), with τ_i values for Nb^{TT} sites slightly larger τ_i than for the rest of the B-cations (Figure 8a). At 600K and 550K, relaxation slows down slightly with the contrast between Nb^{TT} and other sites becoming more pronounced. At the Burns temperature of 500K, the increase in τ_i values for Nb^{TT} sites is accompanied by a jump in τ_i values for many Ti sites, which for the first time reach τ_i values equal to those of Nb^{TT} sites. Thus, although slow dynamics are present for individual sites in the system even at $T > T_b$, these sites are not connected and are slow dynamics isolated at individual point-like (0D) TT dipoles. However, at the Burns temperature for the first time, groups of unit cells nucleated at the Nb^{TT} sites exhibit slow dynamics, giving rise to clusters or networks of slowly responding dipoles in the material.

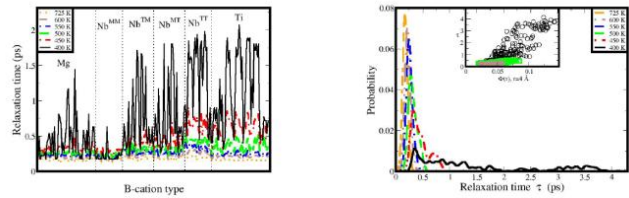


Figure 8. (a) Relaxation time τ_i of individual B-cation sites. At T_b longer relaxation times are first exhibited not only by the Nb^{TT} sites, but also by the Ti sites, indicating the appearance of slow dynamics. (b) Distribution of the relaxation times for the B-sites. The inset shows the relationship between the relaxation time τ_i and the dipole-dipole correlation function $\Phi(r)$ at $r=4\text{Å}$. High $\Phi(r)$ values indicate strong coupling neighbor sites which leads to higher τ_i .

When the temperature is lowered from $T_b=500\text{K}$ to 450K and then 400K, the fraction of the sites with slow dynamics grows rapidly. Slow relaxation spreads first to Nb^{MT} and Nb^{TM} sites (at 450K) and then to Mg and Nb^{MM} sites (at 400K). However, even at the low temperatures, there are still many sites with small τ_i (≈ 0.5 – 1.0 ps) and fast dynamics indicating a gradual transition from fast to slow dynamics between T_b and T_f .

Analysis of τ_i distribution shows, that lowering of temperature leads to a large rise in the average τ_i , a broadening of the τ_i distribution and the divergence of the longest lifetimes (Figure 8b). This is in agreement with phenomenological models of the experimental relaxor dielectric response data^[50,51].

The τ_i distribution in the para-electric phase is a narrow Gaussian centered at $\approx 0.2\text{--}0.3$ ps. At the Burns temperature of 500K, the Gaussian distribution is broader. More importantly, a shoulder at 0.5 ps appears, creating a strong deviation from the Gaussian shape. This shoulder is due to the appearance of sites with slow relaxor dynamics. At 450K, the distinct Gaussian shapes are clearly visible. These peaks are also present at 400K. The first peak remains at a low value of 0.4 ps and does not widen significantly compared to the τ_i distribution at $T > T_b$. This peak is due to the paraelectric matrix sites which exhibit fast dynamics even at 400K. The second and third peaks (roughly at 1 ps and 4 ps, respectively) are broad and are broadened even further to 9 ps at 375K.

Relating ion chemistry and environment to response: Crystal chemistry effects are the origin of strong coupling between Nb^{TT} atoms and their Ti neighbors, which gives rise to slower relaxation observed at the Nb^{TT} sites. Since the O atoms between Nb and Ti are over-bonded, the O-Nb and O-Ti bond lengths are strongly anti-correlated. An Nb^{TT} atom must therefore coordinate its oscillations with its two Ti neighbors, slowing down the dynamics of polarization flipping at the Nb^{TT} site. Examination of the site-resolved real-space dipole-dipole correlation function $\Phi(r)_i$ (Figure 8b, inset) supports this hypothesis. At T_b these sites that exhibit high $\Phi(r)_i$ values (between 0.08 and 0.1) also exhibit large relaxation lifetime magnitudes ($\tau_i > 0.5$ ps). In the PE phase, only a small number of Nb^{TT} sites exhibit high $\Phi(r)_i$ values, and they have a smaller τ_i .

In summary, we find that first-principles-derived atomistic simulations of PMN-PT both exhibit all the dielectric signatures of relaxor behavior, and are amenable to ultra-high resolution spatial and temporal decomposition of this relaxor response. This enables identification of an atomic-scale origin for the relaxor ferroelectric phenomenon.

3. Significance to DoD

Perovskite oxides form the basis for a range of military-relevant technologies such as dielectric ceramics for capacitor applications, ferroelectric thin film non-volatile memories, piezoelectric materials for SONAR and actuators, and electro-optic materials for data storage and displays. A microscopic understanding of perovskite oxides properties is critical for the goal of designing new materials. Once the relationships between the atomic composition, structure and materials properties are understood, new materials that improve upon existing technology can be designed. The US Navy would reap a considerable military advantage from more robust ferroelectric memory impervious to electromagnetic pulse attacks, higher performance SONAR for detection of submarines and photovoltaic materials for energy

generation. Simulations of polarization switching are vital for obtaining guidance for design of efficient and robust non-volatile ferroelectric memory devices, for use in the challenging Navy operating environment. Our atomistic study of ultra-fast switching in PbTiO₃ elucidated the THz dynamics due to an applied electric field pulse, determining the limit of data read/write speed in non-volatile memories. Presenting the first theoretical work on ABS_x, we show that sulfur containing perovskites exhibit a low band gap and can have the potential for use in photovoltaic applications. Our MD simulations have revealed the microscopic origin of relaxor behavior mechanism in PMN-PT which is the basis for the next-generation SONAR devices because of its extraordinarily high electrostrictive constants.

Systems Used

The work presented here was performed using the NAVY Cray XT5, the Engineer Research and Development Center's Cray XT3 and XT4 and the Arctic Region Supercomputer Center's Sun Opteron Cluster and Cray XT5. With regards to both ABINIT and our in-house code, BH, ionic relaxations typically run in about a week on the XT4 and Opteron machines. DFT codes use an iterative diagonalization procedure to solve quantum mechanical calculations that rely heavily on BLAS and LAPACK routines. Typically, runs use 4 to 32 processors. Our in-house code is highly scalable with a parallelization efficiency of almost 100% for a small numbers of processors (<20) and dropping off to slightly above 50% at 128 processors. Calculations using Moldy (an MD program which was developed by Keith Refson under the GNU General Public License) were performed on Cray XT4. Moldy is efficiently parallelized with MPI, with MD simulations usually performed on 32 nodes with a parallelization efficiency of larger than 75 %.

Computational Technology Area

Computational Material Science

Acknowledgements

This work was supported by the Office of Naval Research, under grants N00014-07-1-0409, N00014-09-1-0157, and N00014-06-1-0459, and by the US National Science Foundation, under grant CHE06-16939 and through the MRSEC grant, DMR05-20020. This work was also supported by the US Department of Energy Office of Basic Energy Sciences, under grant number DE-FG02-07ER46431. Computational support was provided by a Challenge Grant from the High Performance

Computing Modernization Office of the US Department of Defense.

References

1. Goldschmidt, V.M., *Die Naturwissenschaften*, 21, 477, 1926.
2. Hohenberg, P. and W. Kohn, *Phys. Rev.*, 136, B864, 1964.
3. Kohn, W. and L.J. Sham, *Phys. Rev.*, 140, A1133, 1965.
4. Qi, T., Y.-H. Shin, K.-L. Yeh, K.A. Nelson, and A.M. Rappe, *Phys. Rev. Lett.*, 102, 247603 1, 2009.
5. Bennett, J.W., I. Grinberg, and A.M. Rappe, *Phys. Rev. B*, 79, 235115, 2009.
6. Grinberg, I., Y.-H. Shin, and A.M. Rappe, *Phys. Rev. Lett.*, 103, 197601, 2009.
7. Nuernerberger, P., G. Vogt, T. Brixner, and G. Gerber, *Phys. Chem. Chem. Phys.*, 9, 2470, 2007.
8. Shi, S. and H. Rabitz, *Chem. Phys.*, 139, 185, 1989.
9. Levis, R.J. and H.A. Rabitz, *J. Phys. Chem.*, 106, 6427, 2002.
10. Wefers, M.M. and K.A. Nelson, *Opt. Lett.*, 20, 1047, 1995.
11. Weiner, A.M., *Rev. Sci. Instrum.*, 71, 1929, 2000.
12. Brixner, T. and G. Gerber, *Opt. Lett.*, 26, 557, 2001.
13. Phillpot, S.R. and V. Gopalan, *Appl. Phys. Lett.*, 84, 1916, 2004.
14. Shin, Y.-H., J.-Y. Son, B.-J. Lee, I. Grinberg, and A.M. Rappe, *Condens. Matter*, 20, 015224, 2008.
15. Shin, Y.-H., I. Grinberg, I.-W. Chen, and A.M. Rappe, *Nature*, 449, 881, 2007.
16. Padilla, J., W. Zhong, and D. Vanderbilt, *Phys. Rev. B*, 53, R5969, 1996.
17. Tybell, T., P. Paruch, T. Giamarchi, and J.-M. Triscone, *Phys. Rev. Lett.*, 89, 097601, 2002.
18. Grigoriev, A., D.H. Do, D.M. Kim, C.B. Eom, B. Adams, E.M. Dufresne, and P.G. Evans, *Phys. Rev. Lett.*, 96, 187601, 2006.
19. Eng, L.M., *Nanotechnology*, 10, 405, 1999.
20. Lindsay, S.J., *Derwent Innovations Index*, edited by US P. Office, US, 2004.
21. McCormick, M.P. and J.C. Larsen, *Feophys. Res. Lett.*, 15, 907, 1988.
22. Kalinin, S.V., C.Y. Johnson, and D.A. Bonnell, *J. Appl. Phys.*, 91, 3816, 2002.
23. Tybell, T., C.H. Ahn, and J.-M. Triscone, *Appl. Phys. Lett.*, 75, 856, 1999.
24. Fahy, S. and R. Merlin, *Phys. Rev. Lett.*, 22, 1122, 1994.
25. Yan, Y.X., E.B. Gamble, and K.A. Nelson, *J. Chem. Phys.*, 83, 5391, 1985.
26. Nelson, K.A., *Coherent control: Optics, molecules, and materials*, Springer-Verlag, Berlin, 1995.
27. Shin, Y.-H., V.R. Cooper, I. Grinberg, and A.M. Rappe, *Phys. Rev. B*, 71, 054104, 2005.
28. Hebling, J., K.-L. Yeh, K.A. Nelson, and M.C. Hoffmann, *IEEE J. Selected Topics in Quantum Electronics*, pp. 345–53, 2008.
29. Juhas, P., I. Grinberg, A.M. Rappe, W. Dmowski, T. Egami, and P.K. Davies, *Phys. Rev. B*, 69, 214101, 2004.
30. Foster, C.M., Z. Li, M. Grimsditch, S.-K. Chan, and D.J. Lam, *Phys. Rev. B*, 48, 10160, 1993.
31. Fukao, S., J.P. McClure, A. Ito, T. Sato, I. Kimura, T. Tsuda, and S. Kato, *Geophys. Res. Lett.*, 15, 768, 1988.
32. Hahn, H. and U. Mutschke, *Z. Anorg. Allg. Chem.*, 288, 269, 1956.
33. Lelieveld, R. and D.J. W. Ijdo, *Acta Cryst.*, B36, 2223, 1980.
34. Nitta, T., K. Nagase, and S. Hayakawa, *J. Am. Ceram. Soc.*, 53, 601, 1970.
35. Wang, Y., N. Sato, K. Yamada, and T. Fujino, *J. Alloys and Compounds*, 311, 214, 2000.
36. Wang, Y., N. Sato, and T. Fujino, *J. Alloys and Compounds*, 327, 104, 2001.
37. Mason, S.E., I. Grinberg, and A.M. Rappe, *Phys. Rev. B Rapid Comm.*, 69, 161401(R), 2004.
38. Bennett, J.W., I. Grinberg, and A.M. Rappe, *Phys. Rev. B*, 73, 180102(R), 2006.
39. Gonze, X., J.-M. Beuken, R. Caracas, F. Detraux, M. Fuchs, G.-M. Rignanese, L. Sindic, M. Verstraete, G. Zerah, F. Jollet, et al., *Comp. Mater. Sci.*, 25, 478, 2002.
40. Monkhorst, H.J. and J. D. Pack, *Phys. Rev. B*, 13, 5188, 1976.
41. Resta, R., *Rev. Mod. Phys.*, 66, 899, 1994.
42. Rappe, A.M., K.M. Rabe, E. Kaxiras, and J.D. Joannopoulos, *Phys. Rev. B Rapid Comm.*, 41, 1227, 1990.
43. Ramer, N.J. and A.M. Rappe, *Phys. Rev. B*, 59, 12471, 1999.
44. <http://opium.sourceforge.net>.
45. Glazer, A.M., *Acta Cryst.*, 28, 3384, 1972.
46. Woodward, P.M., *Acta Cryst.*, B53, 32, 1997.
47. Woodward, P.M., *Acta Cryst.*, B53, 44, 1997.
48. Singh, D.J., *Phys. Rev. B*, 52, 12559, 1995.
49. Viehland, D., S.J. Jang, L.E. Cross, and M. Wuttig, *Phys. Rev. B*, 46, 8003, 1992.
50. Pirc, R., R. Blinc, and V. Bobnar, *Phys. Rev. B*, 63, 054203, 2001.
51. Bovtun, V., S. Veljko, S. Kamba, J. Petzelt, S. Vakhruhev, Y. Yakymenko, K. Brinkman, and N. Setter, *J. Euro. Ceram. Soc.*, 26, 2867, 2006.
52. Akbas, M.A. and P.K. Davies, *J. Am. Ceram. Soc.*, 80, 2933, 1997.